
Anomaly Detection with Conditioned Denoising Diffusion Models

Arian Mousakhan¹ Thomas Brox¹ Jawad Tayyub²

¹University of Freiburg ²Endress+Hauser
{mousakha,brox}@cs.uni-freiburg.de
jawad.tayyub@endress.com

Abstract

Reconstruction-based methods have struggled to achieve competitive performance on anomaly detection. In this paper, we introduce Denoising Diffusion Anomaly Detection (*DDAD*). We propose a novel denoising process for image reconstruction conditioned on a target image. This results in a coherent restoration that closely resembles the target image. Subsequently, our anomaly detection framework leverages this conditioning where the target image is set as the input image to guide the denoising process, leading to defectless reconstruction while maintaining nominal patterns. We localise anomalies via a pixel-wise and feature-wise comparison of the input and reconstructed image. Finally, to enhance the effectiveness of feature comparison, we introduce a domain adaptation method that utilises generated examples from our conditioned denoising process to fine-tune the feature extractor. The veracity of the approach is demonstrated on various datasets including MVTec and VisA benchmarks, achieving state-of-the-art results of 99.5% and 99.3% image-level AUROC respectively.

1 Introduction

Anomaly detection involves the identification and localisation of instances in data that are inconsistent with nominal observations. Detecting out-of-distribution data is a pivotal task in many fields such as industry [4, 49], medicine [48, 24] and video surveillance [27]. In a supervised setting, a model is trained on a dataset with normal and abnormal examples. However, anomalies are usually unforeseen. Methods that model the distribution of non-anomalous samples detect anomalies as patterns that deviate from the nominal distribution. Thus, they can deal with an open set of anomalies and can also spatially localise them.

Representation-based methods [34, 17, 7, 8, 10, 44] rely on features from pretrained neural networks to define the similarity metric for nominal samples and to approach the problem on a nearest neighbor strategy. Reconstruction-based methods learn a generative model from *only* nominal training examples [1, 9, 25]. Ideally, such models can create samples of the whole distribution of nominal samples but are incapable of generating samples that deviate from that distribution. This allows for the detection of anomalies by comparing the anomalous input with its predicted *anomaly-free* reconstruction. However, past methods have suffered from inferior reconstruction quality or insufficient coverage of the nominal distribution, both resulting in erroneous comparisons between the reconstruction and the input image.

Recently, diffusion models [38, 21] have created new opportunities for deep generative models. This paper revisits reconstruction-based anomaly detection harnessing the potential of diffusion models to generate impressive images from the full nominal distribution, as shown in Figure 1. However, a plain application of a diffusion model to anomaly detection is insufficient. Thus, we make the following contributions. First, we propose a conditioning mechanism that guides the diffusion

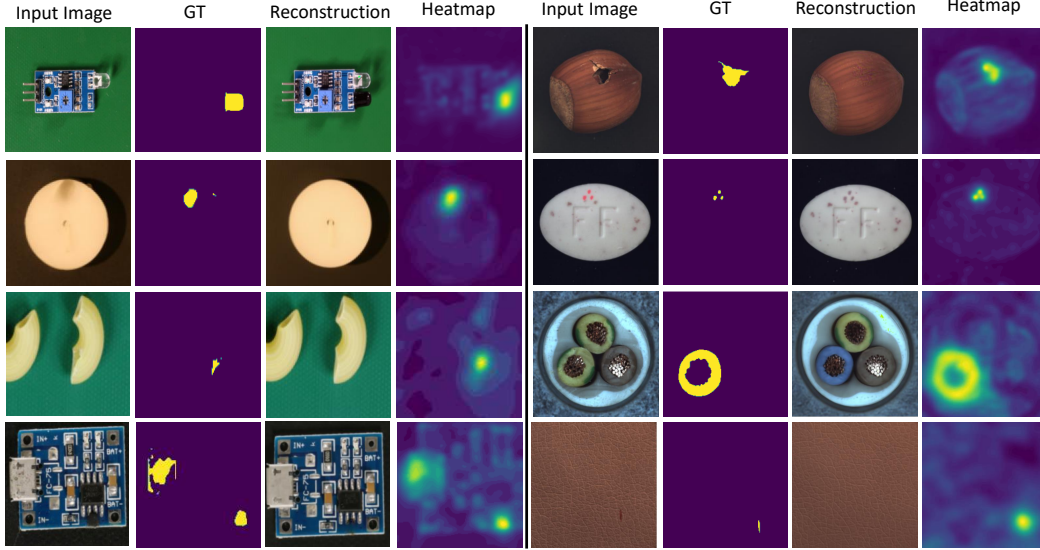


Figure 1: Our approach achieves defect-free reconstruction of input images that are devoid of anomalies. An accurate anomaly detection heatmap is computed. Note that reconstructions are analogous to the expected nominal approximation of the input. In the category of cables, an incorrectly placed green cable has been corrected to the blue one by the model. Such *corrected images* may offer further benefit for industry in repairing defects or worker training.

model’s denoising process to amend each perturbed image until it approximates a target image. This conditioning increases Image AUROC from 89.2% to 92.9% and from 87.6% to 94.2% on MVTEC [4] and VisA [49], respectively. Second, we found that using a combination of a pixel-wise and feature-wise comparison of the conditionally generated image with the input image boosts the detection and localisation of anomalies. Third, we introduce a domain adaptation technique based on the diffusion process. An image, similar to a target image, is first generated using our denoising pipeline. A pretrained feature extractor is then fine-tuned by minimizing the extracted feature distance from the two images. This instills invariance to nominal changes while preserving generality. This feature-based comparison approach with domain adaptation further lifts results to an Image AUROC of 99.3% and 99.5% on MVTEC and VisA, surpassing not only reconstruction-based methods but all state-of-the-art (SOTA) models.

2 Related Work

Representation-based methods Self-supervised learning has been used in the past to learn image features [29, 31, 14], often solving auxiliary tasks. In anomaly detection, [15, 19] have demonstrated that high-quality features facilitate the detection of anomalous samples. DN2 [3] has successfully employed simple ResNets [18], pretrained on Imagenet [36], to extract informative features. Recent approaches such as SPADE [7] use a memory bank of nominal extracted features, PaDiM [8] use locally constrained bag-of-features, PatchCore [34] also use a memory bank and neighborhood-aware patch-level features, CFlow and FastFlow [17, 44] use a generative model called normalizing flow [12, 26] and US and RD4AD [5, 10] use a knowledge distillation method [20] for anomaly detection. All rely on pretrained feature extractors without any adaptation to the domain of the current problem. In this work, we utilise locally aware patch features, as proposed by [34], to improve comparison of input image and its reconstruction at inference time. We propose a method to transfer knowledge of the current domain of feature extractors used in aforementioned models, achieving superior performance.

Reconstruction-based methods The initial frameworks for anomaly detection were based on the foundational concept that a model learns to accurately reconstruct nominal data while failing to reconstruct anomalies. Anomalous data typically deviate significantly from learned patterns leading to a poor reconstruction of anomalies at inference time. An early work [28] applied Variational Autoencoder (VAE) [25] to detect anomalies in skin disease images. However, reconstructions were blurry and anomalies weren't adequately removed. Various techniques have since been proposed, [6] use a perceptual loss based on structural similarity (SSIM) to improve learning. [37] deploy one generative model as a novelty detector connected end-to-end to a second network enhancing the inlier samples and distorted outliers. [32] use an adversarial autoencoder to effectively compute the likelihood of a sample generated by the inlier distribution. However, these methods are only capable of one-class classification and do not localise anomalies. Ganamoly [1] makes use of a conditional GAN [16, 30], outperforming previous state-of-the-art models. [33, 46] for detecting and localizing use a discriminative end-to-end trainable surface anomaly paradigm. However, these models for training rely on synthetic anomalies. Recently, denoising diffusion models have gained popularity for image, and audio [38, 21]. In the medical domain, denoising diffusion models have been used to detect brain tumors [42]. AnoDDPM [43] showed that these models outperform GANs for anomaly detection in the medical domain. DiffusionAD [47], developed contemporaneously with this work, utilises two sub-networks for denoising and segmentation, demonstrating the success of diffusion models in anomaly detection. Our work outperforms previous approaches and showcases the efficacy of diffusion models for anomaly detection.

3 Background

Denoising diffusion models [38, 21] are inspired by non-equilibrium thermodynamics. They are generative models which aim to learn a distribution $p_\theta(\mathbf{x})$ that closely resembles the data distribution $q(\mathbf{x})$. Diffusion models generate latent variables $\mathbf{x}_1, \dots, \mathbf{x}_T$, having the same dimensions as the input data $\mathbf{x}_0 \sim q(\mathbf{x}_0)$, by gradually adding noise $\epsilon \sim \mathcal{N}(0, \mathbf{I})$ at each time step t . This results in \mathbf{x}_T being complete noise normally distributed with mean 0 and variance 1. Given a pre-defined variance schedule $\beta_1 < \beta_2 < \dots < \beta_T$ where $\beta_t \in (0, 1)$, the forward process over a series of T steps is defined as follows:

$$q(\mathbf{x}_{1:T}|\mathbf{x}_0) = \prod_{(t \geq 1)} q(\mathbf{x}_t|\mathbf{x}_{t-1}), \quad q(\mathbf{x}_t|\mathbf{x}_{t-1}) = \mathcal{N}(\mathbf{x}_t; \sqrt{1 - \beta_t}\mathbf{x}_{t-1}, \beta_t\mathbf{I}). \quad (1)$$

Given the additivity property, merging multiple Gaussians results in also a Gaussian distribution. Therefore \mathbf{x}_t is directly computed at an arbitrary time step t as $q(\mathbf{x}_t|\mathbf{x}_0) = \mathcal{N}(\mathbf{x}_t; \sqrt{\alpha_t}\mathbf{x}_0, (1 - \alpha_t)\mathbf{I})$, where $\alpha_t = \prod_{i=1}^t (1 - \beta_i)$. Despite the ease with which noise is introduced to an image, undoing this perturbation is inherently challenging. This is referred to as *reverse process* in DDPM [22] defined by a parameterised function $p_\theta(\mathbf{x}_{t-1}|\mathbf{x}_t) = \mathcal{N}(\mathbf{x}_{t-1}; \mu_\theta(\mathbf{x}_t, t), \beta_t\mathbf{I})$, where the mean is derived using the learnable function $\epsilon_\theta^{(t)}(\mathbf{x}_t)$. DDPM suggests the training objective $\|\epsilon_\theta^{(t)}(\mathbf{x}_t) - \epsilon\|^2$ to train the model.

Denoising Diffusion Implicit Models (DDIM) [39] accelerate upon DDPM by employing a non-Markovian sampling process. DDIM uses an implicit density model rather than an explicit one used in DDPM. DDIM suggests a sampling process $q_\sigma(\mathbf{x}_{t-1}|\mathbf{x}_t, \mathbf{x}_0)$ by defining a new variance schedule. Based on $\mathbf{x}_t = \sqrt{\alpha_t}\mathbf{x}_0 + \sqrt{1 - \alpha_t}\epsilon$, one can predict the denoised observation \mathbf{x}_0 as follows:

$$f_\theta^{(t)}(\mathbf{x}_t) := (\mathbf{x}_t - \sqrt{1 - \alpha_t}\epsilon_\theta^{(t)}(\mathbf{x}_t))/\sqrt{\alpha_t}. \quad (2)$$

Having defined the generative process $p_\theta^{(t)}(\mathbf{x}_{t-1}|\mathbf{x}_t) = q_\sigma(\mathbf{x}_{t-1}|\mathbf{x}_t, f_\theta^{(t)}(\mathbf{x}_t))$, accordingly via $\mathbf{x}_{t-1} = \sqrt{\alpha_{t-1}}f_\theta^{(t)}(\mathbf{x}_t) + \sqrt{1 - \alpha_{t-1} - \sigma_t^2}\epsilon_\theta^{(t)}(\mathbf{x}_t) + \sigma_t\epsilon_t$, where σ_t determines the stochasticity of the sampling process, one can generate new samples. The connection between diffusion models and score matching [40] was introduced by [41] and derived a score-based function to estimate the deviation that should happen at each time step to make a less noisy image. It can be written as:

$$\nabla_{\mathbf{x}_t} \log p_\theta(\mathbf{x}_t) = -\frac{1}{\sqrt{1 - \alpha}}\epsilon_\theta^{(t)}(\mathbf{x}_t), \quad (3)$$

which [11] used to introduce conditional sampling for DDIM. We similarly leverage the score-based function to introduce our conditioned denoising process in the following section.

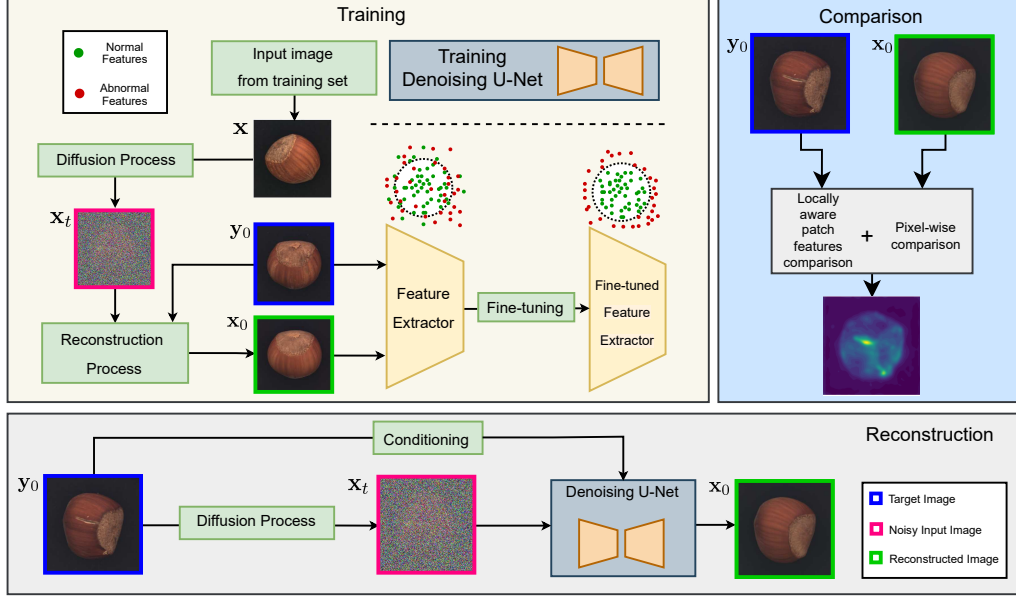


Figure 2: Framework of *DDAD*. After a denoising U-Net has been trained, the feature extractor is adapted to the problem domain by minimising the distance between a target image and a reconstructed image from the training data. At inference time noise is added to the input image and the denoising process is conditioned on the same input image. Finally, the reconstructed image is compared with the input through both pixel and feature matching to generate an accurate anomaly heatmap.

4 Denoising Diffusion Anomaly Detection

In this section, we first present our denoising process for reconstruction. We then explain how sampling is used to eradicate anomalies while preserving nominal information resulting in an anomaly-free image. Finally, we present a robust approach to compare the reconstructed image with the input, resulting in an accurate anomaly localisation. An overview of *DDAD* is presented in Figure 2.

Algorithm 1 Sampling for Reconstruction

```

1:  $\mathbf{x}_{T'} \leftarrow \sqrt{\alpha_{T'}} \mathbf{x} + \sqrt{1 - \alpha_{T'}} \epsilon$ 
2: for all  $t = T', \dots, 1$  do
3:    $\mathbf{y}_t \leftarrow \sqrt{\alpha_t} \mathbf{y}_0 + \sqrt{1 - \alpha_t} \epsilon_{\theta}^{(t)}(\mathbf{x}_t)$ 
4:    $\hat{\epsilon}_t \leftarrow \epsilon_{\theta}^{(t)}(\mathbf{x}_t) - w \sqrt{1 - \alpha_t} (\mathbf{y}_t - \mathbf{x}_t)$ 
5:    $\mathbf{x}_{t-1} \leftarrow \sqrt{\alpha_{t-1}} \hat{f}_{\theta}^{(t)}(\mathbf{x}_t)$ 
    $\quad + \sqrt{1 - \alpha_{t-1} - \sigma_t^2} \hat{\epsilon}_t + \sigma_t \epsilon_t$ 
6: end for
7: return  $\mathbf{x}_0$ 

```

Algorithm 2 Anomaly Scoring

```

1:  $D_p \leftarrow \mathcal{L}_1(\mathbf{x}_0, \mathbf{y}_0)$ 
2:  $D_f \leftarrow 0$ 
3: for all  $j \in J$  do
4:    $D_f \leftarrow D_f + \left(1 - \frac{\phi_j(\mathbf{x}_0)^T \cdot \phi_j(\mathbf{y}_0)}{\|\phi_j(\mathbf{x}_0)\| \|\phi_j(\mathbf{y}_0)\|}\right)$ 
5: end for
6:  $D_p \leftarrow \left(\frac{\max(D_f)}{\max(D_p)}\right) D_p$ 
7:  $D_{anomaly} \leftarrow v D_p + D_f$ 
8: return  $D_{anomaly}$ 

```

4.1 Conditioned Denoising Process for Reconstruction

Given a target image $\mathbf{y}_0 \sim q(\mathbf{y}_0)$ and a perturbed image \mathbf{x}_t , our aim is to denoise \mathbf{x}_t step-by-step to result in an image starkly similar to \mathbf{y}_0 at the end of the trajectory. First, the trained diffusion model predicts noise $\epsilon_{\theta}^{(t)}(\mathbf{x}_t)$ at each timestep t . To nudge the noisy image towards the target image, we add the same noise $\epsilon_{\theta}^{(t)}(\mathbf{x}_t)$ to \mathbf{y}_0 , with the assumption $\mathbf{x}_t \sim \mathbf{y}_t$. Therefore, a condition is imposed on the denoising process by adding \mathbf{y}_t introducing $\nabla_{\mathbf{x}_t} \log p_{\theta}(\mathbf{x}_t | \mathbf{y}_t)$ as the score posterior distribution. Based on Bayes' rule, this decomposes as follows:

$$\nabla_{\mathbf{x}_t} \log p_{\theta}(\mathbf{x}_t | \mathbf{y}_t) = \nabla_{\mathbf{x}_t} \log p_{\theta}(\mathbf{x}_t) + \nabla_{\mathbf{x}_t} \log p_{\theta}(\mathbf{y}_t | \mathbf{x}_t). \quad (4)$$

The unconditional score term $\nabla_{\mathbf{x}_t} \log p_\theta(\mathbf{x}_t)$ can be directly calculated from Equation 3. In many cases calculating the conditional score (or likelihood) $\nabla_{\mathbf{x}_t} \log p_\theta(\mathbf{y}_t|\mathbf{x}_t)$ is intractable. Nevertheless, having calculated \mathbf{y}_t allows for directly computing this likelihood. Intuitively, the likelihood $\nabla_{\mathbf{x}_t} \log p_\theta(\mathbf{y}_t|\mathbf{x}_t)$ can be viewed as a correction score for a deviation that occurs in \mathbf{x}_t from \mathbf{y}_t at each denoising step. Knowing that both \mathbf{x}_t and \mathbf{y}_t consist of the same noise, this deviation is only present at the image (signal) level. Consequently, we calculate the divergence by $\mathbf{y}_t - \mathbf{x}_t$, and an adjusted noise term $\hat{\epsilon}$ is computed as follows:

$$\hat{\epsilon} = \epsilon_\theta^{(t)}(\mathbf{x}_t) - w\sqrt{1 - \alpha_t}(\mathbf{y}_t - \mathbf{x}_t), \quad (5)$$

where w controls the temperature of the conditioning. Given $\hat{\epsilon}$, the new prediction $\hat{f}_\theta^{(t)}(\mathbf{x}_t)$ is calculated using Equation 2, resulting in \mathbf{x}_0 converging towards the target image \mathbf{y}_0 . Finally, the less-noisy image \mathbf{x}_{t-1} is calculated in the sampling process as follows:

$$\mathbf{x}_{t-1} = \sqrt{\alpha_{t-1}}\hat{f}_\theta^{(t)}(\mathbf{x}_t) + \sqrt{1 - \alpha_{t-1} - \sigma_t^2}\hat{\epsilon} + \sigma_t\epsilon_t. \quad (6)$$

The summary of our denoising process is shown in 1.

4.2 Reconstruction for Anomaly Detection

For anomaly detection tasks, the target image \mathbf{y}_0 is set as the input image \mathbf{x} . This enables to generate an anomaly-free approximation of \mathbf{x} through denoising which has been conditioned on \mathbf{y}_0 . Since the model is only trained on nominal data, anomalous regions lie in the low probability density of $p_\theta(\mathbf{x})$. Therefore, during denoising, the reconstruction of anomalies falls behind the nominal part. Over an entire trajectory, earlier steps focus on the abstract picture of the image whereas later steps aim to reconstruct fine-grained details. Since anomalies mostly emerge at a fine level, the initial time step can be set as $T' < T$, where a sufficient amount of signal-to-noise ratio is present. Note that the model is trained on complete trajectories. We label our model as *DDAD- n* , where n refers to the number of denoising iterations.

4.3 Anomaly Scoring

In the simplest case, we can detect and localise anomalies via the pixel-wise \mathcal{L}_1 norm between the input and its reconstruction. However, we found it beneficial to additionally utilise perceptual similarity metrics [47, 13]. Concretely, given a reconstructed image \mathbf{x}_0 and the target image \mathbf{y}_0 , we define a pixel-wise distance function D_p and a feature-wise distance function D_f to derive the anomaly heatmap. D_p is calculated based on the \mathcal{L}_1 norm in pixel space. At the feature level, similar to PatchCore [34] and PaDiM [8], we utilise adaptive average pooling to spatially smooth each individual feature map. Information of each feature within a given patch is aggregated in a single representation, resulting in the same dimensionality as the input feature. A cosine similarity is utilised to define D_f as:

$$D_f(\mathbf{x}_0, \mathbf{y}_0) = \sum_{j \in J} \left(1 - \frac{\phi_j(\mathbf{x}_0)^T \cdot \phi_j(\mathbf{y}_0)}{\|\phi_j(\mathbf{x}_0)\| \|\phi_j(\mathbf{y}_0)\|} \right). \quad (7)$$

It is applied to the feature extractor ϕ with $j \in \{2, 3\}$ to retain the generality of the used features [34]. We normalise the pixel-wise distance D_p to share the same upper bound as the feature-wise distance D_f . Consequently, the final anomaly score function is a combination of the pixel and the feature distance:

$$D_{anomaly} = \left(v \frac{\max(D_f)}{\max(D_p)} \right) D_p + D_f, \quad (8)$$

where v controls the importance of the pixel-wise distance. Algorithm 2 details this method.

4.4 Domain Adaptation

In subsection 4.3 we use a pretrained feature extractor for feature-wise comparison between an input image and its reconstruction. However, these networks are trained on ImageNet and do not adapt well to domain-specific characteristics of an anomaly detection task. We propose a domain-adaptation method by converging different layers extracted from two similar images of the training set. We first sample a random image \mathbf{x} and perturb it with noise to obtain \mathbf{x}_t . We also randomly select a target

image y_0 . Given a trained denoising model θ , a noisy image x_t is denoised to x_0 that approximates y_0 . Features are extracted from the reconstructed and target image, denoted as $\phi_j(x_0)$ and $\phi_j(y_0)$, where ϕ refers to a pretrained feature extractor [45, 18] and $j \in J$ is the set of layers considered. The knowledge of the network ϕ is then transferred to $\hat{\phi}$. A cosine similarity is employed, similar to Equation 7, for each of the final activation layers of the j^{th} spatial resolution block. For our experiments, J is set as $\{1, 2, 3\}$ layers. This results in a feature extractor that is resilient to slight changes. As shown in Figure 5, it helps the model to become robust to the nominal variation of the object and background after reconstruction.

5 Experiments

5.1 Datasets and Evaluation Metrics

We demonstrate the veracity of our proposed framework on three datasets: MVTec, VisA and MTD. We adopt the 1-class protocol for evaluation on all datasets. The MVTec Anomaly Detection benchmark [4] is a widely known industrial dataset comprising of 15 sub-datasets with 5 categories of textures and 10 of objects. Each category contains anomaly-free samples for training and various anomalous samples for testing ranging from small scratches to large missing components. We also evaluate on a newly published dataset called VisA [49] which is twice the size of MVTec comprising of 9,621 normal and 1,200 anomalous high-resolution images. Images exhibit complex structures, objects placed in sporadic locations, and different objects. Anomalies include scratches, dents, color spots, cracks, and structural defects. For both these benchmarks, we trained the denoising network on images of size 256×256 and, for comparison, images were cropped to 224×224 . Other than these, we also experimented on Magnetic Tile Defects (MTD) dataset [23]. This dataset is a single-category dataset with 925 nominal training images and 5 sub-categories of different types of defects totaling 392 test images. We use 80% of defect-free images as the training set. No data augmentation is applied to any dataset, since the augmentation transformations may be actual anomalies.

We assess the efficacy of our model by utilizing the Area Under Receiver Operator Characteristics (AUROC) metric, both at the image and pixel level. At the image level, we determine the maximum anomaly score across pixels and assign it as the overall anomaly score of the image. Based on the calculated anomaly scores, we conduct a one-class classification to calculate the image-level AUROC for anomaly detection. For a more comprehensive evaluation of localisation performance, we use the Per Region Overlap (PRO) metric [5]. The PRO score treats anomaly regions of varying sizes equally, making it a more robust metric than pixel AUROC.

Table 1: Anomaly Classification and localisation performance (image AUROC, pixel AUROC) of various methods on VisA benchmark. The best results are highlighted in bold.

Method	Representation-based				Reconstruction-based	
	SPADE [7]	PaDiM[8]	RD4AD[10]	PatchCore[34]	DRAEM [46]	DDAD-10
Candle	(91.0,97.9)	(91.6,98.6)	(92.2,97.9)	(98.6, 99.5)	(91.8,96.6)	(99.9 ,98.4)
Capsules	(61.4,60.7)	(70.7,97.4)	(90.1,89.5)	(81.6,99.5)	(74.7,98.5)	(97.9 , 99.6)
Cashew	(97.8,86.4)	(93.0,98.5)	(99.6 ,95.8)	(97.3, 98.9)	(95.1,83.5)	(98.4,93.0)
Chewing gum	(85.8,98.6)	(98.8,98.9)	(99.7 ,99.0)	(99.1, 99.1)	(94.8,96.8)	(99.0,97.6)
Fryum	(88.6,96.7)	(88.6,95.4)	(96.6,94.3)	(96.2,93.8)	(97.4 ,87.2)	(98.8 ,93.6)
Macaroni1	(95.2,96.2)	(87.0,99.1)	(98.4,97.7)	(97.5,99.8)	(97.2, 99.9)	(100 ,99.3)
Macaroni2	(87.9,87.5)	(70.5,96.5)	(97.6,87.7)	(78.1,99.1)	(85.0, 99.2)	(99.2 , 99.2)
PCB1	(72.1,66.9)	(94.7,99.3)	(97.6,75.0)	(98.5, 99.9)	(47.6,88.7)	(99.9 ,94.3)
PCB2	(50.7,71.1)	(88.5,98.7)	(91.1,64.8)	(97.3, 99.0)	(89.8,91.3)	(99.2 ,97.0)
PCB3	(90.5,95.1)	(91.0,98.7)	(95.5,92.8)	(97.9, 99.2)	(92.0,98.0)	(100 ,98.1)
PCB4	(83.1,89.0)	(97.5,96.5)	(96.5,92.8)	(99.6, 98.6)	(98.6,96.8)	(99.9 ,98.3)
Pipe fryum	(81.1,81.8)	(97.0, 99.3)	(97.0,92.0)	(99.8,99.1)	(100 ,98.8)	(99.8,96.5)
Average	(82.1,85.6)	(89.1,98.1)	(96.0,96.5)	(95.1, 98.8)	(88.7,93.5)	(99.3 ,97.0)

5.2 Experimental Setting

We use the modified UNet proposed in [11] to train our denoising model. The model is trained for 2000 epochs with Adam optimiser, a learning rate of 0.0003, weight decay of 0.05, and a batch

Table 2: A detailed comparison of Anomaly Classification and localisation performance of various methods on MVTec benchmark [4] in the format of (image AUROC, pixel AUROC). The five rows represent the category of textures and the rest nine rows represent the category of objects.

Method	Representation-based			Reconstruction-based				
	CFlow[17]	RD4AD[10]	PatchCore[34]	GANomaly [1]	AE [6]	SkipG [2]	DRAEM [46]	DDAD-10
Carpet	(100,98.3)	(98.9,98.9)	(98.7,98.9)	(20.3,-)	(50,-)	(70.9,-)	(97.0,95.5)	(97.8,98.0)
Grid	(97.6,99.0)	(100,99.3)	(99.7,98.3)	(40.4,-)	(78.0,-)	(47.7,-)	(99.9,99.7)	(100,99.6)
Leather	(97.7,99.7)	(100,99.4)	(100,99.3)	(41.3,-)	(44.0,-)	(60.9,-)	(100,98.6)	(100,99.3)
Tile	(98.7,98.0)	(99.3,95.6)	(100,99.3)	(40.8,-)	(77.0,-)	(29.9,-)	(99.6,99.2)	(100,98.5)
Wood	(99.6,96.7)	(99.2,95.3)	(99.2,95.0)	(74.4,-)	(74.0,-)	(19.9,-)	(99.1,96.4)	(99.8,96.8)
Bottle	(100,99.0)	(100,98.7)	(100,98.6)	(25.1,-)	(80.0,-)	(85.2,-)	(99.2,99.1)	(100,98.9)
Cable	(100,97.6)	(95.0,97.4)	(99.5,98.4)	(45.7,-)	(56.0,-)	(54.4,-)	(91.8,94.7)	(99.7,98.4)
Capsule	(99.3,99.0)	(96.3,98.7)	(98.1,98.8)	(68.2,-)	(62.0,-)	(54.3,-)	(98.5,94.3)	(98.1,96.2)
Hazelnut	(96.8,98.9)	(99.9,98.9)	(100,98.7)	(53.7,-)	(88.0,-)	(24.5,-)	(100,99.7)	(99.9,99.0)
Metal nut	(91.9,98.6)	(100,97.3)	(100,98.4)	(27.0,-)	(73.0,-)	(81.4,-)	(98.7,99.5)	(99.0,96.8)
Pill	(99.9,99.0)	(96.6,98.2)	(99.8,98.9)	(47.2,-)	(62.0,-)	(67.1,-)	(98.9,97.6)	(98.6,99.2)
Screw	(99.7,98.9)	(97.0,99.6)	(98.1,99.4)	(23.1,-)	(69.0,-)	(87.9,-)	(93.9,97.6)	(99.5,99.4)
Toothbrush	(95.2,99.0)	(99.5,99.1)	(100,98.7)	(37.2,-)	(98.0,-)	(58.6,-)	(100,98.1)	(100,98.9)
Transistor	(99.1,98.0)	(96.7,92.5)	(100,96.3)	(44.0,-)	(71.0,-)	(84.5,-)	(93.1,90.9)	(99.6,92.6)
Zipper	(98.8,99.1)	(98.5,98.2)	(99.4,98.8)	(43.4,-)	(80.0,-)	(76.1,-)	(100,98.8)	(100,98.6)
Average	(98.3,98.6)	(98.5,97.8)	(99.1,98.1)	(42.1,-)	(63.0,-)	(60.2,-)	(98.0,97.3)	(99.5,98.1)

Table 3: AUROC results of Anomaly Detection on MTD [23]

MTD	GANomaly [1]	DifferNet[35]	PatchCore-10 [34]	DDAD-10
Image AUROC	76.7	97.7	97.9	98.3

Table 4: PRO metric for anomaly localisation on MVTec AD [4] and VisA [49] dataset. The best results are highlighted in bold.

Method	SPADE [7]	PaDiM[8]	RD4AD[10]	PatchCore[34]	DDAD-10
VisA	65.9	85.9	70.9	91.2	91.3
MVTec	91.7	92.1	93.9	93.5	92.9

size of 32. For feature extractor fine-tuning, Adam optimiser with a learning rate of 0.0001 is used. Moreover, each batch is split into two mini-batches of size 16 each, where one comprises of input images and the other has target images. These are needed for domain adaptation. The number of epochs for fine-tuning, often between zero and four, depends on the amount of available training data. The trade-off between pixel-wise and feature-wise distance is set to $v = 7$ and the conditioning control parameter is set as $w = 4$ for the denoising process and to $w = 3$ when fine-tuning the feature extractor. A sensitivity analysis of w is presented in Figure 3. We empirically determine that the noising time step is set to $T' = 200$ as it strikes a favourable balance between signal and noise. A Gaussian filter with $\sigma = 4$ is leveraged to smooth the anomaly heatmaps. All experiments have been conducted on a GeForce RTX 3090.

5.3 Experimental Results and Discussions

Anomaly detection results on VisA and MVTec and MTD datasets are shown in Table 1, Table 2 and Table 3 respectively. Our proposed framework *DDAD* outperforms all existing approaches, not only the reconstruction-based ones but also representation-based, achieving the highest Image AUROC in all datasets. The proposed use of diffusion models enables anomaly detection and localisation based on generative modeling, which has been a longstanding idea, with problems in practice for anomaly detection. Plain diffusion models alone are not sufficient to lift reconstruction-based methods up to a competitive level. This is shown by the ablation study on the VisA dataset in Figure 4, where various components of the presented framework are removed. Ablations with MVTec are added to the supplementary section. Without conditioning, performance drops by 3.7% and 6.6% on MVTec and VisA, respectively. The use of diffusion-based domain adaptation adds 2.3% and 15.5% to feature-wise comparison, and adds 5.7% and 4.0% to the final performance on MVTec and VisA

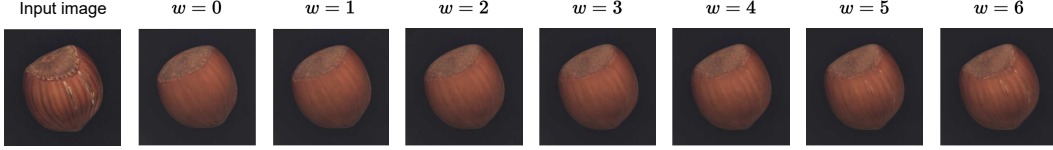


Figure 3: Effect of conditioning parameter on reconstruction

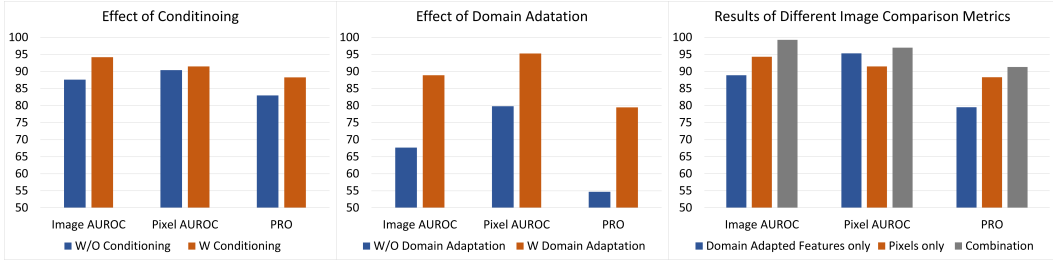


Figure 4: Effectiveness of various components of our model on anomaly detection and segmentation. Left: Effectiveness of conditioning based on pixel-wise image comparison. Middle: Performance increase due to domain adaptation of feature extractor. Right: Impact of merging feature-wise and pixel-wise image comparison. All results are shown on VisA [49] dataset.

respectively. Furthermore, the use of both pixels and features-based image comparison achieves the highest performance. *DDAD*'s performance on the PRO metric is presented in Table 4. *DDAD* achieves SOTA results on VisA and competitive results to PaDiM [8] and PatchCore [34] in MVTec. The inferior pixel-level performance compared to image-level performance can be attributed to initial denoising point $T' = 200$, which presents a greater challenge to reconstruct large missing components (such as transistor). However, starting from earlier time steps further introduces ambiguities in the reconstruction and leads to increased inference time. Some failure modes of the model are presented in the supplementary section.

Figure 1 and Figure 5 present the qualitative results obtained for reconstruction and anomaly segmentation. It is noteworthy how accurately anomalies are localized in various samples from the VisA and MVTec datasets. The model's reconstruction predictions are particularly remarkable, as they not only segment anomalous regions but also transform them into their nominal counterparts. For instance, the model regenerates missing links on transistors, erases blemishes on circuit boards, and recreates missing components on PCBs. These reconstructions hold significant value in industrial settings, as they provide valuable insights to workers, enabling them to identify defects and potentially resolve them. More detailed quantitative and qualitative results are included in the supplementary.

5.4 Inference Time

The trade-off between accuracy and computation time on the VisA dataset is depicted in Table 5. Among the tested approaches, *DDAD-10* stands out by utilizing 10 iterations and delivering the most favorable results. However, *DDAD-5* becomes an appealing option due to its faster inference time, which holds significant importance, especially in industrial applications. With the exception of *DDAD-3*, the denoising process is initiated at time step $T' = 200$ with varying number of denoising networks applied to accelerate reconstruction. For *DDAD-3*, we found that starting the denoising process from time step $T' = 120$ is beneficial. Although this approach offers a desirable reduction in iterations, there is a significant drop in accuracy. *DDAD-20* is not as precise as *DDAD-10* in anomaly localisation as well as being slower, however, performs marginally better in anomaly detection.

Table 5: Inference time per image and performance of the model on VisA [49] with different number of denoising steps in the format of (Image AUROC, Pixel AUROC, PRO).

Method	DDAD-3	DDAD-5	DDAD-10	DDAD-20
Performance	(92.1,90.1,80.5)	(98.2,95.8,90.7)	(99.3,97.0,91.3)	(99.5,95.8,90.8)
Time (s)	0.11	0.17	0.33	0.65

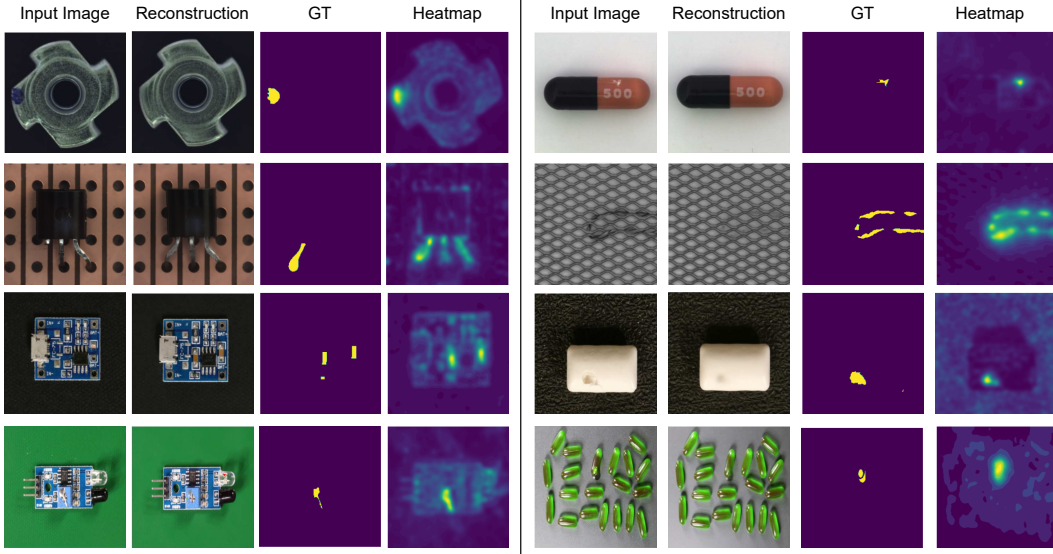


Figure 5: First and second rows depict samples on 'metal nut', 'capsule', 'transistor', and 'grid' selected from MVTec [4]. Third and forth rows depict samples of 'pcb4', 'chewing gum', 'pcb3' and 'capsules' selected from VisA [49].

6 Conclusion

We have introduced Denoising Diffusion Anomaly Detection (*DDAD*), a new reconstruction-based approach for detecting anomalies. Our model leverages the impressive generative capabilities of recent diffusion models to perform anomaly detection. We design a conditioned denoising process to generate an anomaly-free image that closely resembles a target image. This results in our model being up to two hundred times faster than DDPM. Moreover, we propose an image comparison method based on pixel and feature matching for accurate anomaly localisation. Finally, we introduced a novel technique that utilises our denoising model to adapt a pretrained neural network to the problem's domain for expressive feature extraction. *DDAD* achieves state-of-the-art results on benchmark datasets, namely MVTec, VisA, and MTD, *despite* being a reconstruction-based method.

Limitations and future work. In this work, we have shown that starting with a lower amount of noise and fewer denoising steps accelerates inference time while achieving promising performance. However, we observed the failure of the model in the reconstruction of anomalies which are large missing components. This results in an inaccurate anomaly segmentation. Selecting multiple starting points for denoising could mitigate these issues. Also training our model in the latent space would bring benefits in speed and localisation quality. We leave these intriguing avenues for future experimentation.

References

- [1] Samet Akcay, Amir Atapour-Abarghouei, and Toby P Breckon. Ganomaly: Semi-supervised anomaly detection via adversarial training. In *Computer Vision-ACCV 2018: 14th Asian Conference on Computer*

- Vision, Perth, Australia, December 2–6, 2018, Revised Selected Papers, Part III 14*, pages 622–637. Springer, 2019.
- [2] Samet Akçay, Amir Atapour-Abarghouei, and Toby P Breckon. Skip-ganomaly: Skip connected and adversarially trained encoder-decoder anomaly detection. In *2019 International Joint Conference on Neural Networks (IJCNN)*, pages 1–8. IEEE, 2019.
 - [3] Liron Bergman, Niv Cohen, and Yedid Hoshen. Deep nearest neighbor anomaly detection. *arXiv preprint arXiv:2002.10445*, 2020.
 - [4] Paul Bergmann, Michael Fauser, David Sattlegger, and Carsten Steger. Mvtec ad—a comprehensive real-world dataset for unsupervised anomaly detection. In *Proceedings of the IEEE/CVF conference on computer vision and pattern recognition*, pages 9592–9600, 2019.
 - [5] Paul Bergmann, Michael Fauser, David Sattlegger, and Carsten Steger. Uninformed students: Student-teacher anomaly detection with discriminative latent embeddings. In *Proceedings of the IEEE/CVF conference on computer vision and pattern recognition*, pages 4183–4192, 2020.
 - [6] Paul Bergmann, Sindy Löwe, Michael Fauser, David Sattlegger, and Carsten Steger. Improving unsupervised defect segmentation by applying structural similarity to autoencoders. *arXiv preprint arXiv:1807.02011*, 2018.
 - [7] Niv Cohen and Yedid Hoshen. Sub-image anomaly detection with deep pyramid correspondences. *arXiv preprint arXiv:2005.02357*, 2020.
 - [8] Thomas Defard, Aleksandr Setkov, Angelique Loesch, and Romaric Audigier. Padim: a patch distribution modeling framework for anomaly detection and localization. In *Pattern Recognition. ICPR International Workshops and Challenges: Virtual Event, January 10–15, 2021, Proceedings, Part IV*, pages 475–489. Springer, 2021.
 - [9] David Dehaene and Pierre Eline. Anomaly localization by modeling perceptual features. *arXiv preprint arXiv:2008.05369*, 2020.
 - [10] Hanqiu Deng and Xingyu Li. Anomaly detection via reverse distillation from one-class embedding. In *Proceedings of the IEEE/CVF Conference on Computer Vision and Pattern Recognition*, pages 9737–9746, 2022.
 - [11] Prafulla Dhariwal and Alexander Nichol. Diffusion models beat gans on image synthesis. *Advances in Neural Information Processing Systems*, 34:8780–8794, 2021.
 - [12] Laurent Dinh, Jascha Sohl-Dickstein, and Samy Bengio. Density estimation using real NVP. In *International Conference on Learning Representations*, 2017.
 - [13] Alexey Dosovitskiy and Thomas Brox. Generating images with perceptual similarity metrics based on deep networks. *Advances in neural information processing systems*, 29, 2016.
 - [14] Spyros Gidaris, Praveer Singh, and Nikos Komodakis. Unsupervised representation learning by predicting image rotations. *arXiv preprint arXiv:1803.07728*, 2018.
 - [15] Izhak Golan and Ran El-Yaniv. Deep anomaly detection using geometric transformations. In S. Bengio, H. Wallach, H. Larochelle, K. Grauman, N. Cesa-Bianchi, and R. Garnett, editors, *Advances in Neural Information Processing Systems*, volume 31. Curran Associates, Inc., 2018.
 - [16] Ian Goodfellow, Jean Pouget-Abadie, Mehdi Mirza, Bing Xu, David Warde-Farley, Sherjil Ozair, Aaron Courville, and Yoshua Bengio. Generative adversarial networks. *Communications of the ACM*, 63(11):139–144, 2020.
 - [17] Denis Gudovskiy, Shun Ishizaka, and Kazuki Kozuka. Cflow-ad: Real-time unsupervised anomaly detection with localization via conditional normalizing flows. In *Proceedings of the IEEE/CVF Winter Conference on Applications of Computer Vision*, pages 98–107, 2022.
 - [18] Kaiming He, Xiangyu Zhang, Shaoqing Ren, and Jian Sun. Deep residual learning for image recognition. In *Proceedings of the IEEE conference on computer vision and pattern recognition*, pages 770–778, 2016.
 - [19] Dan Hendrycks, Mantas Mazeika, Saurav Kadavath, and Dawn Song. Using self-supervised learning can improve model robustness and uncertainty. *Advances in neural information processing systems*, 32, 2019.
 - [20] Geoffrey Hinton, Oriol Vinyals, and Jeff Dean. Distilling the knowledge in a neural network. *arXiv preprint arXiv:1503.02531*, 2015.

- [21] Jonathan Ho, Ajay Jain, and Pieter Abbeel. Denoising diffusion probabilistic models. *Advances in Neural Information Processing Systems*, 33:6840–6851, 2020.
- [22] Jonathan Ho, Ajay Jain, and Pieter Abbeel. Denoising diffusion probabilistic models. In H. Larochelle, M. Ranzato, R. Hadsell, M.F. Balcan, and H. Lin, editors, *Advances in Neural Information Processing Systems*, volume 33, pages 6840–6851. Curran Associates, Inc., 2020.
- [23] Yibin Huang, Congying Qiu, and Kui Yuan. Surface defect saliency of magnetic tile. *The Visual Computer*, 36:85–96, 2020.
- [24] Jeremy Irvin, Pranav Rajpurkar, Michael Ko, Yifan Yu, Silvana Ciurea-Ilcus, Chris Chute, Henrik Marklund, Behzad Haghighi, Robyn Ball, Katie Shpanskaya, et al. Chexpert: A large chest radiograph dataset with uncertainty labels and expert comparison. In *Proceedings of the AAAI conference on artificial intelligence*, volume 33, pages 590–597, 2019.
- [25] Diederik P Kingma and Max Welling. Auto-encoding variational bayes. *arXiv preprint arXiv:1312.6114*, 2013.
- [26] Durk P Kingma and Prafulla Dhariwal. Glow: Generative flow with invertible 1x1 convolutions. *Advances in neural information processing systems*, 31, 2018.
- [27] Wen Liu, Weixin Luo, Dongze Lian, and Shenghua Gao. Future frame prediction for anomaly detection—a new baseline. In *Proceedings of the IEEE conference on computer vision and pattern recognition*, pages 6536–6545, 2018.
- [28] Yuchen Lu and Peng Xu. Anomaly detection for skin disease images using variational autoencoder. *arXiv preprint arXiv:1807.01349*, 2018.
- [29] Michael Mathieu, Camille Couprie, and Yann LeCun. Deep multi-scale video prediction beyond mean square error. *arXiv preprint arXiv:1511.05440*, 2015.
- [30] Mehdi Mirza and Simon Osindero. Conditional generative adversarial nets. *arXiv preprint arXiv:1411.1784*, 2014.
- [31] Mehdi Noroozi and Paolo Favaro. Unsupervised learning of visual representations by solving jigsaw puzzles. In *Computer Vision—ECCV 2016: 14th European Conference, Amsterdam, The Netherlands, October 11–14, 2016, Proceedings, Part VI*, pages 69–84. Springer, 2016.
- [32] Stanislav Pidhorskyi, Ranya Almohsen, and Gianfranco Doretto. Generative probabilistic novelty detection with adversarial autoencoders. *Advances in neural information processing systems*, 31, 2018.
- [33] Nicolae-Cătălin Ristea, Neelu Madan, Radu Tudor Ionescu, Kamal Nasrollahi, Fahad Shahbaz Khan, Thomas B Moeslund, and Mubarak Shah. Self-supervised predictive convolutional attentive block for anomaly detection. In *Proceedings of the IEEE/CVF Conference on Computer Vision and Pattern Recognition*, pages 13576–13586, 2022.
- [34] Karsten Roth, Latha Pemula, Joaquin Zepeda, Bernhard Schölkopf, Thomas Brox, and Peter Gehler. Towards total recall in industrial anomaly detection. In *Proceedings of the IEEE/CVF Conference on Computer Vision and Pattern Recognition*, pages 14318–14328, 2022.
- [35] Marco Rudolph, Bastian Wandt, and Bodo Rosenhahn. Same same but different: Semi-supervised defect detection with normalizing flows. In *Proceedings of the IEEE/CVF winter conference on applications of computer vision*, pages 1907–1916, 2021.
- [36] Olga Russakovsky, Jia Deng, Hao Su, Jonathan Krause, Sanjeev Satheesh, Sean Ma, Zhiheng Huang, Andrej Karpathy, Aditya Khosla, Michael Bernstein, et al. Imagenet large scale visual recognition challenge. *International journal of computer vision*, 115:211–252, 2015.
- [37] Mohammad Sabokrou, Mohammad Khaloee, Mahmood Fathy, and Ehsan Adeli. Adversarially learned one-class classifier for novelty detection. In *Proceedings of the IEEE conference on computer vision and pattern recognition*, pages 3379–3388, 2018.
- [38] Jascha Sohl-Dickstein, Eric Weiss, Niru Maheswaranathan, and Surya Ganguli. Deep unsupervised learning using nonequilibrium thermodynamics. In *International Conference on Machine Learning*, pages 2256–2265. PMLR, 2015.
- [39] Jiaming Song, Chenlin Meng, and Stefano Ermon. Denoising diffusion implicit models. In *International Conference on Learning Representations*, 2021.

- [40] Yang Song and Stefano Ermon. Generative modeling by estimating gradients of the data distribution. *Advances in neural information processing systems*, 32, 2019.
- [41] Yang Song, Jascha Sohl-Dickstein, Diederik P Kingma, Abhishek Kumar, Stefano Ermon, and Ben Poole. Score-based generative modeling through stochastic differential equations. In *International Conference on Learning Representations*, 2021.
- [42] Julia Wolleb, Florentin Bieder, Robin Sandkühler, and Philippe C Cattin. Diffusion models for medical anomaly detection. In *Medical Image Computing and Computer Assisted Intervention–MICCAI 2022: 25th International Conference, Singapore, September 18–22, 2022, Proceedings, Part VIII*, pages 35–45. Springer, 2022.
- [43] Julian Wyatt, Adam Leach, Sebastian M Schmon, and Chris G Willcocks. Anoddpm: Anomaly detection with denoising diffusion probabilistic models using simplex noise. In *Proceedings of the IEEE/CVF Conference on Computer Vision and Pattern Recognition*, pages 650–656, 2022.
- [44] Jiawei Yu, Ye Zheng, Xiang Wang, Wei Li, Yushuang Wu, Rui Zhao, and Liwei Wu. Fastflow: Unsupervised anomaly detection and localization via 2d normalizing flows. *arXiv preprint arXiv:2111.07677*, 2021.
- [45] Sergey Zagoruyko and Nikos Komodakis. Wide residual networks. *arXiv preprint arXiv:1605.07146*, 2016.
- [46] Vitjan Zavrtanik, Matej Kristan, and Danijel Skočaj. Draem-a discriminatively trained reconstruction embedding for surface anomaly detection. In *Proceedings of the IEEE/CVF International Conference on Computer Vision*, pages 8330–8339, 2021.
- [47] Richard Zhang, Phillip Isola, Alexei A Efros, Eli Shechtman, and Oliver Wang. The unreasonable effectiveness of deep features as a perceptual metric. In *Proceedings of the IEEE conference on computer vision and pattern recognition*, pages 586–595, 2018.
- [48] David Zimmerer, Jens Petersen, Gregor Köhler, Paul Jäger, Peter Full, Klaus Maier-Hein, Tobias Roß, Tim Adler, Annika Reinke, and Lena Maier-Hein. Medical out-of-distribution analysis challenge 2022, March 2022.
- [49] Yang Zou, Jongheon Jeong, Latha Pemula, Dongqing Zhang, and Onkar Dabeer. Spot-the-difference self-supervised pre-training for anomaly detection and segmentation. In *Computer Vision–ECCV 2022: 17th European Conference, Tel Aviv, Israel, October 23–27, 2022, Proceedings, Part XXX*, pages 392–408. Springer, 2022.

A Implementation Details

The code is implemented in Python 3.8 and PyTorch 1.13. We explored ResNet50 [18], WideResNet50, and WideResNet101 [45] as options for the feature extractor. However, all reported results are based on the pretrained WideResNet101. The σ parameter for the denoising process is set equal to 1. Empirically, we achieved the same results in employing a denoising process that is either probabilistic or implicit. Nevertheless, it is essential to note that changing this hyperparameter affects reconstruction and may require additional hyperparameter tuning.

B Additional Quantitative results

B.1 Dependency on conditioning and comparison metrics on MVTec

As demonstrated in Section 5.3, our conditioning approach significantly improves the performance of the model compared to plain diffusion models. This improvement on MVTec [4] is also evident in Figure 6, where the image AUROC, pixel AUROC, and PRO metrics have increased 4.7%, 1.7%, and 3.4% respectively using the pixel-wise comparison. While only pixel-wise comparison achieves promising results of 98.5%, the overall performance raises to 99.5% after combination with feature-wise comparison. Additionally, the performance of the feature-wise comparison has shown a remarkable improvement after domain adaptation.

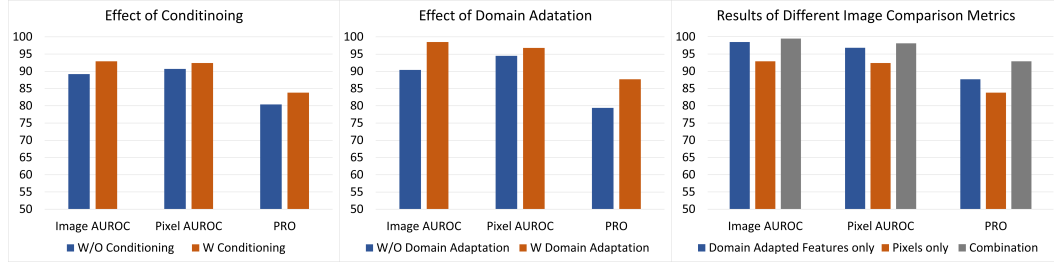


Figure 6: Effectiveness of various components of our model on anomaly detection and segmentation. Left: Effectiveness of conditioning based on pixel-wise image comparison. Middle: Performance increase due to domain adaptation of feature extractor. Right: Impact of merging feature-wise and pixel-wise image comparison. All results are shown on MVTec [4] dataset.

B.2 Detailed results on the PRO metric

In this section, we present detailed results on VisA [49] and MVTec [4]. Results on the PRO metric and comparison with the other approaches are depicted in Table 6 and Table 7.

Table 6: Anomaly Localization Performance on MVTec [4], based on PRO metric.

Categories	Carpet	Grid	Leather	Tile	Wood	Bottle	Cable	Capsule	Hazelnut	Metal nut	Pill	Screw	Toothbrush	Transistor	Zipper	Avg
SPADE [7]	94.7	86.7	97.2	75.9	87.4	95.5	90.9	93.7	95.4	94.4	94.6	96.0	93.5	87.4	92.6	91.7
PaDiM [8]	96.2	94.6	97.8	86.0	91.1	94.8	88.8	93.5	92.6	85.6	92.7	94.4	93.1	84.5	95.9	92.1
RD4AD [10]	97.0	97.6	99.1	90.6	90.9	96.6	91.0	95.8	95.5	92.3	96.4	98.2	94.5	78.0	95.4	93.9
PatchCore [34]	96.6	95.9	98.9	87.4	89.6	96.1	92.6	95.5	93.9	91.3	94.1	97.9	91.4	83.5	97.1	93.5
DDAD-10	91.0	98.5	98.3	96.7	90.0	94.8	90.9	90.7	87.3	91.8	95.6	92.0	95.0	87.2	94.1	92.9

Table 7: Anomaly Localization Performance on VisA [49], based on PRO metric.

Categories	Candle	Capsules	Cashew	Chewing gum	Fryum	Macaroni1	Macaroni2	PCB1	PCB2	PCB3	PCB4	Pipe fryum	Avg
SPADE [7]	93.2	36.1	57.4	93.9	91.3	61.3	63.4	38.4	42.2	80.3	71.6	61.7	65.9
PaDiM [8]	95.7	74.9	87.9	83.5	80.2	92.1	75.4	91.3	88.7	84.9	81.6	92.5	85.9
RD4AD [10]	92.2	56.9	79.0	92.5	81.0	71.9	68.0	43.2	46.4	80.3	72.2	68.3	70.9
PatchCore [34]	94.0	85.5	94.5	84.6	95.3	95.4	94.4	94.3	89.2	90.9	90.1	95.7	91.2
DDAD-10	95.2	99.6	80.5	84.4	93.3	99.1	98.5	94.4	90.6	95.2	92.3	85.2	91.3

B.3 Influence of different denoising steps

This section focuses on the detailed performance analysis of each category within the DDAD framework, considering different denoising steps. We provide the results for Anomaly Detection and Anomaly Localization on the Visa dataset [49], presented in Table 8 and Table 9 respectively.

Table 8: Anomaly Detection Performance (Image AUROC) on VisA [49], based on various denoising steps.

Categories	Candle	Capsules	Cashew	Chewing gum	Fryum	Macaroni1	Macaroni2	PCB1	PCB2	PCB3	PCB4	Pipe fryum	Avg
DDAD-3	93.4	95.6	74	95.4	86.8	99.6	83.7	81.9	100	99.3	99.4	95.7	92.1
DDAD-5	99.9	97.8	90.2	99.7	97.6	99.6	97.0	99.6	99.3	99.2	99.3	99.9	98.2
DDAD-10	99.9	97.9	98.4	99.0	98.8	100	99.2	99.9	99.2	100	99.9	99.8	99.3
DDAD-20	99.8	99.8	98.8	100	98.2	100	99.4	99.5	100	100	99.3	99.6	99.5

Table 9: Anomaly Localization Performance (Pixel AUROC, PRO) on VisA [49], based on various denoising steps.

Categories	Candle	Capsules	Cashew	Chewing gum	Fryum	Macaroni1	Macaroni2	PCB1	PCB2	PCB3	PCB4	Pipe fryum	Avg
DDAD-3	(89.0,66.8)	(97.8,88.2)	(88.7,81.0)	(91.1,69.0)	(77.7,76.8)	(94.9,95.5)	(88.8,86.7)	(87.9,76.3)	(97.2,92.4)	(95.8,89.7)	(95.2,83.2)	(77.2, 60.8)	(90.1, 80.5)
DDAD-5	(98.2,95.6)	(99.3,94.5)	(92.1,83.4)	(92.7,79.4)	(91.2,91.6)	(99.0,98.6)	(98.4,98.1)	(91.5,89.8)	(97.5,92.2)	(97.7,94.3)	(97.3,89.0)	(95.0,81.9)	(95.8, 90.7)
DDAD-10	(98.4,95.2)	(99.6,95.7)	(93.0,80.5)	(97.6,84.4)	(93.6,93.3)	(99.3,99.1)	(99.2,98.5)	(94.3,94.4)	(97.0,90.6)	(98.1,95.2)	(98.3,92.3)	(86.5,80.9)	(96.5,91.3)
DDAD-20	(97.8,95.0)	(99.7,96.4)	(90.4,78.0)	(93.0,79.8)	(89.5,90.0)	(99.4,99.3)	(99.3,99.5)	(91.9,91.9)	(97.5,91.5)	(98.1,95.4)	(97.4,88.3)	(96.3,85.0)	(95.8, 90.8)

C Additional Qualitative results

C.1 Effect of conditioning on reconstruction

This section offers qualitative results demonstrating the significance of our conditioning contribution for anomaly detection. When conditioning is removed, the nominal region of the image deviates from its original pattern. It may decrease the precision of localization and the nominal region may be considered as abnormal. The impact of conditioning on reconstruction is illustrated in Figure 7. By conditioning the input image, the model achieves better reconstruction of the nominal part while effectively identifying and reconstructing anomalies. In the provided example, the first row displays a sample from the *pill* category of the MVTec dataset [4], where red dots are often randomly distributed. A plain diffusion model fails to reconstruct the dots accurately. However, by increasing the conditioning parameter w , the model successfully reconstructs these red dots. Simultaneously, the anomaly (represented by the yellow color) is eliminated and replaced with the nominal pattern. In the second row, an example of cable is demonstrated, where the plain diffusion correctly changes the color of the top grey cable to green. However, when compared to the conditioned reconstruction, where the wires are accurately reconstructed, the plain diffusion model fails to correctly reconstruct the individual wires within the cable. In the third row, there is an example of a printed part, indicated by a red box, on the pill that is not successfully reconstructed using plain diffusion model. However, when conditioning is applied, the printed part is restored to its original form. In the case of the *hazelnut*, plain diffusion model results in a rotated reconstruction, which is incorrect. When conditioning is applied, the rotation is effectively corrected, and the hazelnut is reconstructed in the right orientation. Additionally, the rays on the hazelnut are reconstructed similarly to the input image, maintaining their original appearance. The last row showcases an example from the VisA dataset [49]. After reconstruction, some nominal information, indicated by the red boxes, are removed. By conditioning the model on the input image, this missing information is brought back, and the model correctly reconstructs those areas. The conditioning mechanism prevents these changes from being falsely identified as anomalous patterns, ensuring accurate reconstruction.

C.2 Robustness to anomalies on the background

In industrial and production settings, one significant challenge often encountered is the presence of anomalies such as dust on the background during photography. In this section, we demonstrate the robustness of the domain-adapted feature extractor to such spurious patterns. As shown in Figure 8, a pretrained feature extractor mistakenly identifies these normal background elements, indicated by the blue boxes, as anomalies. However, through domain adaptation, the feature extractor becomes resilient and no longer misidentifies or mislocates these elements. In the first three rows, we provide

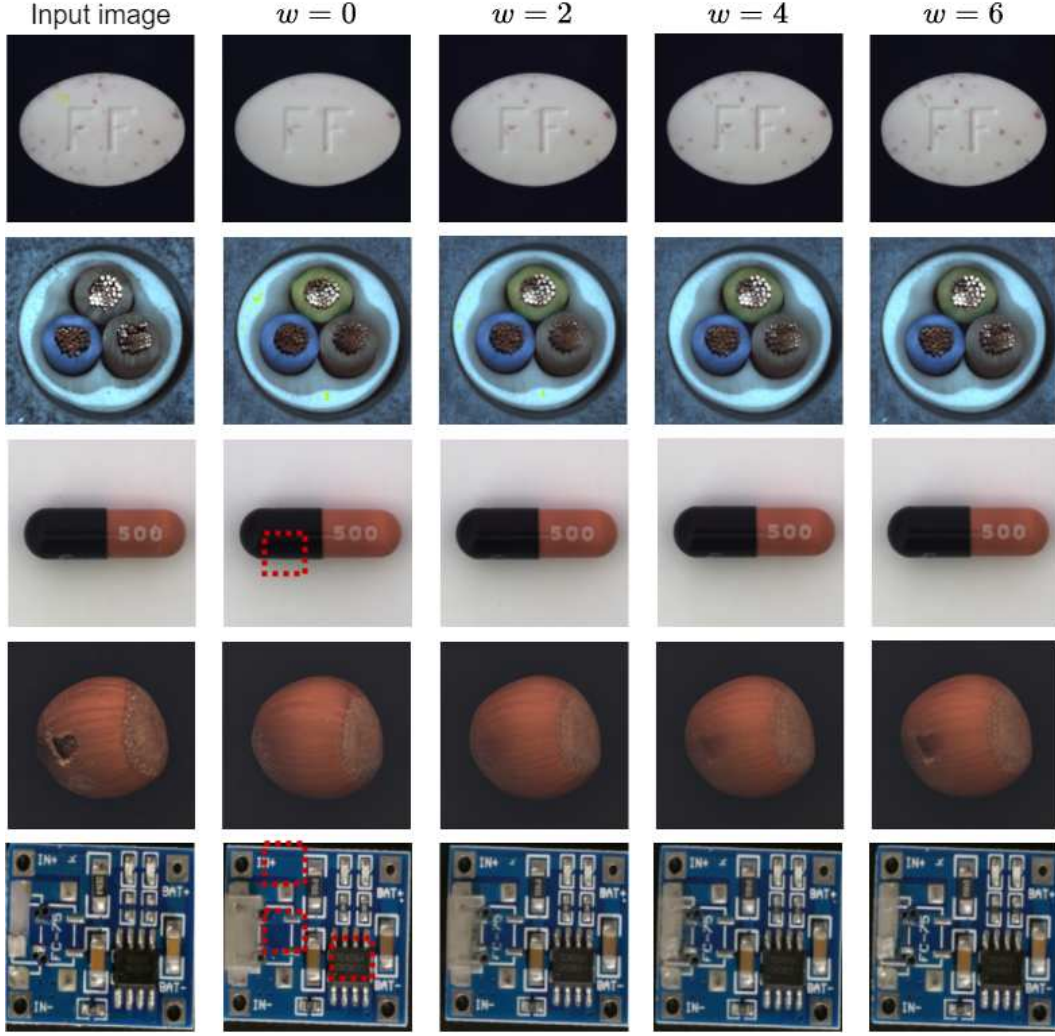


Figure 7: Some qualitative results, showcasing the insufficiency of plain diffusion models for more accurate anomaly detection.

samples from PCB categories and pill, where not only anomalies are mislocalised, but the images are also misclassified.

C.3 Mislocalisation

Although our model achieved a high AUROC for anomaly detection, it faced challenges in accurately localise extreme rotations or figure alterations. For example, as depicted in Figure 9, when starting from time step 200, the model struggled to reconstruct these substantial changes. Conversely, beginning from larger time steps made the reconstruction process difficult and slow. Additionally, it is important to note that our conditioning approach aims to preserve the overall structure of the image similar to the input image. However, in cases where there are drastic changes such as rotations or figure alterations, the conditioning mechanism may lead to mislocalization.

C.4 Qualitative results on MTD

To showcase the versatility of our model beyond the MVTec [4] and VisA [49] datasets, we also evaluated *DDAD* performance on a different dataset called MTD [23]. This evaluation allows us to

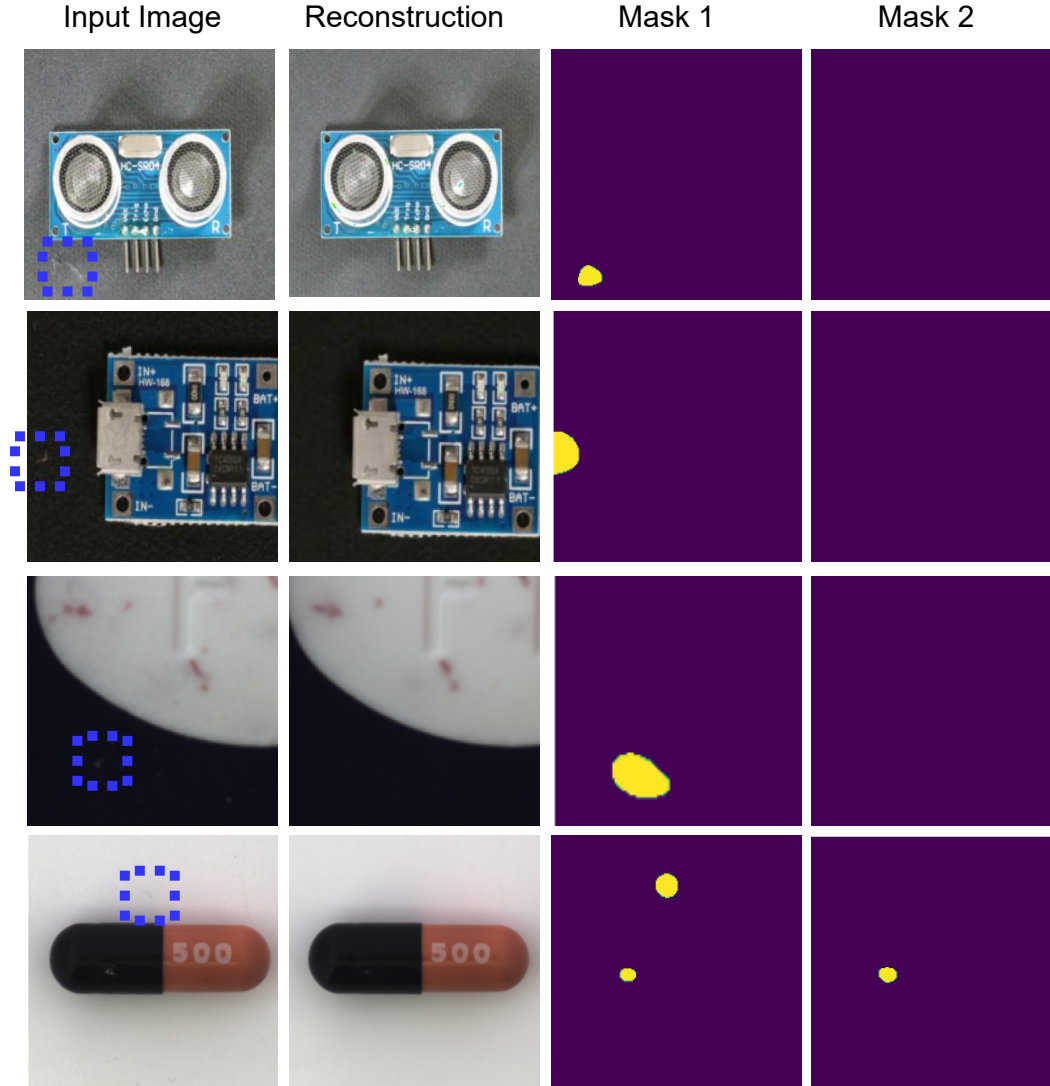


Figure 8: Some qualitative results where the background patterns are considered as anomalies when a pretrained feature extractor is used. It is shown by Mask 1 in Figure. After domain adaptation, the feature extractor becomes robust to these changes. It is shown by Mask 2 in the Figure.

demonstrate the potential of our model across diverse datasets. In Figure 10, we present qualitative results illustrating the performance of our *DDAD* approach on the MTD dataset.

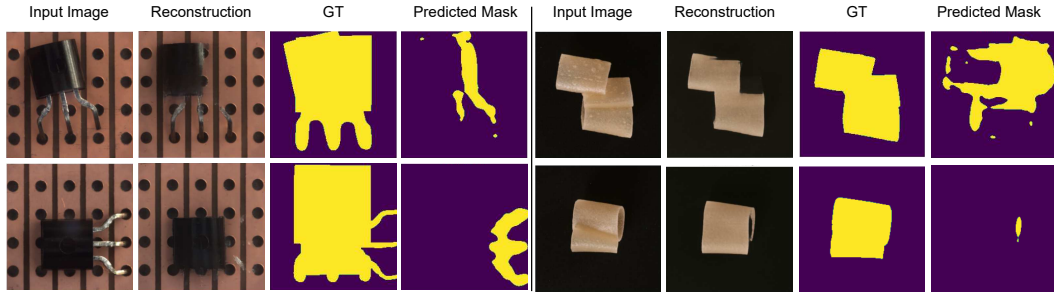


Figure 9: Transistor samples from MVTec [4] and pipe flange examples from [49]. While the images are correctly classified, there is a huge mislocalisation.

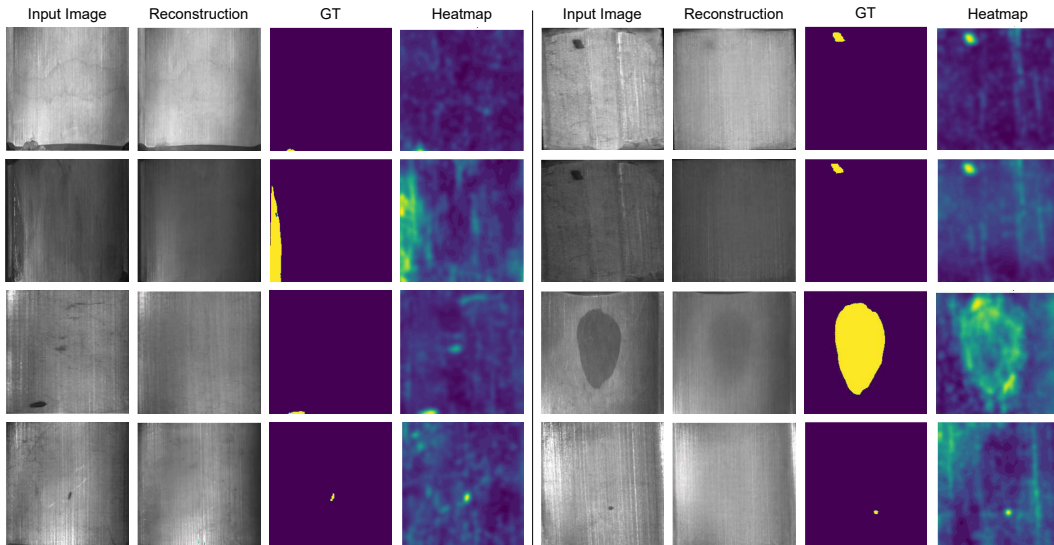


Figure 10: MTD dataset [23].